Hindawi
Geofluids
Volume 2023, Article ID 2070913, 17 pages
https://doi.org/10.1155/2023/2070913

Research Article

Nanopore Characteristics of the Cambrian Niutitang Formation Organic-Rich Shales in the Middle Yangtze Region and Its Formation Controlling Factors

Jie Xu,[1] **Weihua Guo**,[2] **Bin Yang**,[1] **Dongxu Ma**,[1] **Li Zhao**,[1] **Haotian Liu**,[3] **Hongjie Ji**,[4] **and Huifei Tao**[5]

[1]*Bailie School of Petroleum Engineering, Lanzhou City University, Lanzhou, Gansu 730000, China*
[2]*Research Institute of Petroleum Exploration & Development-Northwest, PetroChina, Lanzhou, Gansu 730000, China*
[3]*Exploration and Development Research Institute, SINOPEC Jianghan Oilfield, Wuhan, Hubei 430040, China*
[4]*State Key Laboratory for Nuclear Resources and Environment, East China University of Technology, Nanchang, China*
[5]*Oil and Gas Research Center, Northwest Institute of Eco-Environment and Resources, CAS, Lanzhou, Gansu 730000, China*

Correspondence should be addressed to Huifei Tao; taohuifei@nieer.ac.cn

Received 24 August 2022; Revised 28 October 2022; Accepted 28 November 2022; Published 22 February 2023

Academic Editor: Dengke Liu

The shale of Cambrian Niutitang Formation is one of the most important shale gas reservoirs in the Middle Yangtze region, South China. Nanopores are important reservoir spaces for shale gas. The study of pore characteristics and its formation controlling factors is of great significance for the exploration and development of shale gas in the Niutitang Formation. In this study, two drilling core samples and two profile samples were investigated. The laser Raman, X-ray diffraction analysis, FE-SEM, and low-pressure N_2 and CO_2 adsorption methods are used to study the geochemical and mineral compositions of the shales, and the nanopore characteristics and its formation controlling factors of the shales are discussed. Results show that the shales have the following features: (1) rich in organic matter (OM) and the total organic carbon (TOC) contents ranging from 2.65 to 11.33%, with an average value of 6.81%. (2) The main mineral components of these shales are quartz, feldspar, clay minerals, calcite, and a small amount of pyrite. (3) The samples from the center of the Middle Yangtze region (EY1 well and BGP profile) have a higher maturity value ($_{Rmc}R_0\% = 4.0\%$) relatively to the samples from the south of the Middle Yangtze region (XD1 well and JF profile), where the $_{Rmc}R_0\%$ is 2.8%. (4) The maximum N_2 adsorption capacity of the four groups of shale samples ranges from 5.090 to 27.333 cm^3/g, with an average value of 15.571 cm^3/g, while the maximum CO_2 adsorption capacity ranges from 2.686 to 5.567 cm^3/g, with an average value of 3.776 cm^3/g. The higher maturity leads to the EY1 well having the lowest average maximum N_2 adsorption capacity, while most of the OM pores in the EY1 well and BGP profile samples are smaller than 10 nm in diameter. The tectonic uplift leads to the profile samples having more meso-macropores than the core samples. The dissolution pores and granular mineral support are the key factors for the better pore structure of the high-evolution stage Niutitang Formation shale.

1. Introduction

Shale gas is a different kind of gas accumulations from conventional gas, which exists primarily as the adsorbed gas, free gas, or dissolved gas in the organic-rich shales [1]. Nanopores are the main storage spaces for shale gas, and the nanopore volume and structure are one of the key internal factors affecting the occurrence state of shale gas [2]. Meanwhile, the characteristics of organic matter (such as organic matter content, type, and maturity) and mineral composition of organic-rich shale greatly affect the volume and structure of the pores [3–6]. Although previous studies provided a lot of detailed information on the pore structure in organic-rich shale, the key influencing factor is diverse in different shales because of its inherent heterogeneity [7–10].

The Cambrian Niutitang Formation (CNF) in South China is a favorable horizon for shale gas development because of its high total organic carbon (TOC) contents, high thermal maturities, and wide distribution [11, 12]. Many scholars have studied the nanopore characteristics of the CNF organic-rich shales in the Upper Yangtze region. The CNF shales from Chongqing City with an Eq-Ro of 3.5%-4.2% have a poorer pore development compared with the CNF shales from Yichang City with an Eq-Ro of 1.6%-2.8% [13, 14]. Therefore, some researchers argued that the thermal evolution degree of shale is the key factor for controlling shale pore development in the CNF [14]. Xi et al. [15] studied the pore characterization and the controls of OM and quartz on CNF pore structure in the northern Guizhou Province and thought that the TOC content is the key influencing factor. The shales of the CNF are also widely distributed in the Middle Yangtze region (Figure 1), but the pore characteristics and their influencing factors are still unclear which impeded the development of shale gas in South China.

In this study, we selected core and outcrop samples of the CNF in the Middle Yangtze area and then conducted geochemical analysis, mineralogy, and porosity measurement. We have compared the variation of TOC contents, maturity, lithology, and pore development in the different samples. The main aims of this study are to (1) finely elucidate nanopore characteristics of the CNF organic-rich shale in the Middle Yangtze area and (2) determine the key controls of the nanopores. Our experimental findings would be beneficial to the exploration and development of the CNF shale gas in the Middle Yangtze region.

2. Materials and Methods

2.1. Investigated Samples. The shale samples investigated in this study were collected from drilling cores and outcrops, comprising the Jiangfeng (JF) and Baiguoping (BGP) outcrop profiles and the EY1 and XD1 wells (Figure 1(b)). The JF profile is located in Youyang County, Chongqing City. This section has a total thickness of 27 meters, with a bottom of 3 meters of black siliceous mudstone and 4 meters of black siliceous mudstone and 20 m of black carbonaceous mudstone on the top. A total of 36 samples were collected from this section. The BGP profile is located in Hefeng County, Hubei Province. This section has a total thickness of 57 meters, including 34 meters of black carbonaceous mudstone (Figure 1(c)). 30 samples were collected from this section. To ensure that the lithological and geochemical characteristics of these samples are not affected by weathering, all section samples are fresh samples. The EY1 well is located in Lichuan City, Hubei Province. The Lower Cambrian strata were drilled to depths of 3717-3965 m. A total of 55 samples were collected from this well. The XD1 well is located in Zhangjiajie City, Hunan Province. The Lower Cambrian strata were drilled to depths of 1792.8-1998 m. 30 samples were taken from this well. Ultimately, a total of 24 carbonaceous shales from the core and profile samples were selected for the experimental study (Table 1).

2.2. Experiments. The TOC contents of the samples were tested by CCS-902 series carbon and sulfur analyzer produced by Beijing Wanliandaxinke Instrument Co., Ltd. The pulverized samples were treated with 8% hydrochloric acid to remove carbonates.

In this study, we adopted a HORIBAHR-LabRAM fully automatic microlaser Raman spectrometer to characterize the samples' maturity. In this experiment, a silicon wafer was used as a wave number calibration of Raman instrument. Some other experimental parameters can be consulted in Liu et al. [16].

The nanoporous signatures of the samples were studied by gas adsorption and FE-SEM observation. The gas adsorption included low-pressure N_2 and CO_2 adsorption measurements using a Micromeritics ASAP 2020 HD88 apparatus. Before the gas adsorption test, about 0.25 g of 60~80-mesh powder sample was placed into a vacuum oven and dried at 110°C for 12 hours to remove adsorbed moisture and volatile matters from the sample. The tested pores range from 1.083 nm to 400 nm in the isothermal N_2 adsorption including some microporous, all of the mesoporous, and a part of macroporous. The test temperature was -196°C, and the relative pressure (P/P_0) was 0.000 1~0.995. The low-pressure CO_2 isothermal adsorption was used to determine the microporous signatures. The CO_2 adsorption analysis was carried out at 0°C with a relative pressure P/P_0 ranging from 0.00003 to 0.03. The Brunauer-Emmett-Teller model (BET) was used for calculating the surface area (A_S, m^2/g), the Barrett-Joyner-Halenda (BJH) model was used for calculating pore volume (V_{N2}, cm^3/g), and the density functional theory (DFT) was used to calculate the varied ranges of pore size distributions in these experiments. The nanoporous observation was conducted by field emission scanning electron microscopy (Zeiss, Merlin Compact). The samples were cut into small cubes of 0.5~1 cm^3 at Gatan Precision and then polished by argon ion for 1 hour at an accelerating voltage of 7 kV to produce a flat surface on Gatan Precision Etching Coating System II (PECSII) 685 system. After that, the samples were put into the scanning electroscope for observation with a 1 kV acceleration voltage and 5-6 mm working distances.

At the same time, all the samples were also subjected to X-ray diffraction analysis. These analyses were performed on an Empyrean X-ray diffractometer using Cu Ka radiation at 40 kV and 40 mA. Each scan was performed from 5° to 45° with a step interval of 0.02° at a rate of 2.0°/min.

3. Results

3.1. Organic Geochemistry

3.1.1. Total Organic Carbon (TOC) Contents. Organic matter in shale is the material basis for hydrocarbon generation. Its abundance is an important organic geochemical parameter to evaluate the merits of shale gas reservoirs. This is because it not only directly determines the hydrocarbon generation potential of shale but also produces abundant nanoscale micropores and fractures in the process of hydrocarbon generation, which provides good storage space for shale gas [17,

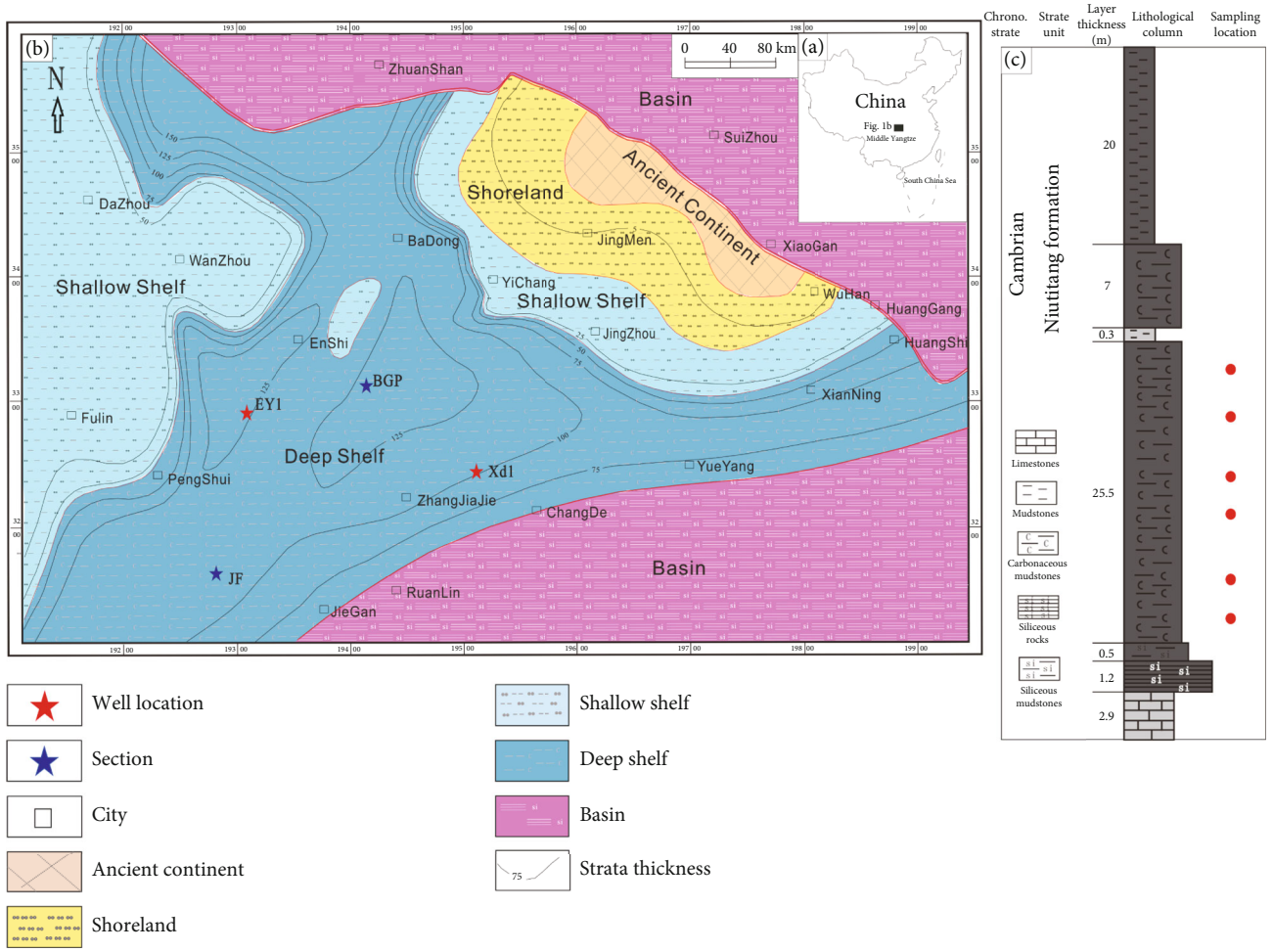

Figure 1: (a) The geographical location of the study area in China. (b) Sedimentary face map of the Cambrian Niutitang Formation in the Middle Yangtze region. (c) The Lithological column of the Niutitang Formation in the BGP section.

18]. The CNF shale is famous for its richness of oil-prone kerogen, but it contains scarce soluble organic matter because of its overmaturity. Thus, in this study, the TOC content is used as a parameter to evaluate the abundance of organic matter. To clarify the relationship between the TOC and pore development of shale in the CNF, the samples which were tested by gas adsorption and FE-SEM were also tested for TOC contents simultaneously. The results are shown in Table 1.

The TOC contents of EY1 well samples range from 4.9 to 10.24 wt. %, with an average of 7.42 wt. %, while the TOC contents of XD1 well samples range from 2.65 to 6.83 wt. %, with an average of 4.84 wt. %. And for the profile samples, the TOC contents of BGP vary from 4.62 to 11.33 wt. %, with an average of 6.64 wt. %, while the TOC contents of JF vary from 6.22 to 8.56 wt. %, with an average of 7.49 wt. %.

3.1.2. Maturity of Organic Matter. Maturity is an important index for source rock evaluation and an important basis for shale oil and gas exploration and development [1, 3, 19, 20]. The maturity evaluation of most organic shales is characterized by vitrinite reflectance of organic matter (VR_o, %) or solid bitumen reflectivity (BR_o, %; [21]). However, the CNF organic-rich shales are overmatured marine shales for which effective maturity indicators are scarce/absent [22, 23]. At the same time, Raman spectroscopy has been increasingly used to determine the maturity of shale because of its simple operation and reliable data [24–27]. Raman measurements can offer a useful maturity proxy mainly via Raman band separation (RBS) calculated from the wavenumbers of the G and D bands [25, 28]. Therefore, in this study, we used the laser Raman spectrum to measure the maturity of the CNF shale.

Details of this test were as follows: firstly, one or two samples from each well or section were selected for Raman spectroscopy analysis. Then, tests were carried out at four different locations of each sample. Some Raman spectra are shown in Figure 2. Liu et al. [16] proposed that the Raman spectra of all kinds of solid organic matter in the stratum have D and G peaks with different morphological intensities and morphologies, which increase with the increase of the thermal evolution degree of the samples, and their peak spacing ($d(G-D)$) and peak height ratio ($h(Dh/Gh)$) change laws are very similar. Meanwhile, they proposed that the peak-to-height ratio can be used to calculate the thermal evolution degree for high to overmature shale. So, finally, the

Table 1: Geochemical characteristics and mineralogical composition of the samples.

Source	Sample no.	Depth (m)	TOC (%)	$_{Rmc}R_0$ (%)	Minerals				
					Quartz	Feldspar	Clay mineral	Calcite	Pyrite
Core samples	EY1-05	3906.1	7.97	—	25	19	47	4	1
	EY1-10	3896.9	7.40	4.07	31	31	32	0	2
	EY1-15	3885.3	10.24	—	25	32	38	2	2
	EY1-18	3879.6	4.99	—	42	42	5	6	5
	EY1-25	3865.8	10.16	—	41	46	6	3	5
	EY1-30	3855.2	6.56	—	12	52	6	4	3
	EY1-35	3845.6	5.83	—	32	33	33	1	2
	EY1-45	3825.4	7.25	—	27	35	30	2	6
	EY1-50	3815.0	8.29	4.06	30	40	18	7	3
	EY1-54	3807.5	5.47	—	26	36	31	1	6
	XD1-70	1923.7	6.83	—	66	21	8	3	2
	XD1-92	1945.8	2.65	2.71	3	0	9	85	3
	XD1-107	1961.5	5.71	—	23	0	9	67	1
	XD1-132	1984.8	4.20	—	26	56	15	0	4
Outcrop samples	BGP-7	—	11.33	—	55	12	26	0	5
	BGP-9	—	7.94	—	56	9	23	4	7
	BGP-12	—	5.66	3.99	62	8	19	6	6
	BGP-13	—	5.49	—	64	11	23	0	2
	BGP-15	—	4.79	—	64	10	21	0	4
	BGP-17	—	4.62	—	38	10	50	0	2
	JF-04	—	6.22	—	60	15	14	0	8
	JF-14	—	8.56	2.73	62	13	18	0	7
	JF-26	—	7.23	2.99	76	5	14	1	4
	JF-36	—	7.96	—	71	5	24	0	0

maturity of samples was calculated through Equation (1), which was proposed by Liu et al. [16] based on Raman parameters. The results of Raman spectrum maturity ($_{Rmc}R_0$%) are shown in Table 1.

$$_{Rmc}R_0\% = 1.1659h(\mathrm{Dh/Gh}) + 2.7588, \quad (1)$$

where $_{Rmc}R_0$% is the reflectance calculated by Raman analysis parameters and h(Dh/Gh) is the peak-to-height ratio (Dh is D peak height, and the Gh is G peak height).

It could be seen from the test results that the CNF shales in the Middle Yangtze are overmature. The shale maturity of the CNF in the JF profile and XD1 well is slightly low with the $_{Rmc}R_0$% to be about 2.8% and 2.7%, respectively, while that of the BGP profile and EY1 well is as high as about 4%.

3.2. Mineral Composition. The mineral compositions of the shale play an important role in the study of shale reservoirs. Shale gas mainly occurs in adsorbed and free states in reservoirs [19]. According to previous studies, clay minerals are important storage places for adsorbed shale gas. The large pore size intergranular pores and contact edge fractures between different minerals formed during diagenesis are the main storage spaces for free shale gas [9, 29–31].

The main mineral components of the CNF shale in the study area are quartz, feldspar, clay minerals, calcite, and a small amount of pyrite (Table 1 and Figure 3). The quartz contents range from 3 to 76 wt. %, with an average of 42 wt. %. The feldspar contents vary from 0 to 56 wt. %, with a mean of 23 wt. %. The clay mineral contents vary from 5 to 50 wt. %, with a mean of 22 wt. %. The calcite contents vary from 0 to 85 wt. %, with a mean of 8 wt. %. But overall, the core samples had lower quartz contents and higher feldspar and calcite contents. The outcrop samples had higher quartz contents and lower feldspar and calcite contents. However, there are no significant differences in the average clay mineral contents between the core samples and the outcrop samples.

3.3. FE-SEM Observations. The classification of shale pores proposed by Loucks et al. [18] and Ko et al. [4] was adopted in this study. We observed organic matter (OM) pores, interparticle (interP) pores, intraparticle (intraP) pores, and microfractures in the samples by the FE-SEM (Figures 4 and 5). OM pores refer to various forms of pores developed in primary organic matter and solid asphalt. The interP pores refer to the pores between all kinds of plastic minerals (such as clay minerals, fecal pellets, and organic matter) and brittle minerals (quartz, feldspar, carbonate minerals, pyrite, etc.). The intraP pores include the strawberry intercrystalline pores of pyrite, interlayer pores of clay minerals, and dissolution pores. The fractures include the structural fractures, diagenetic contraction fractures, and cleavage fractures. Furthermore, the pores

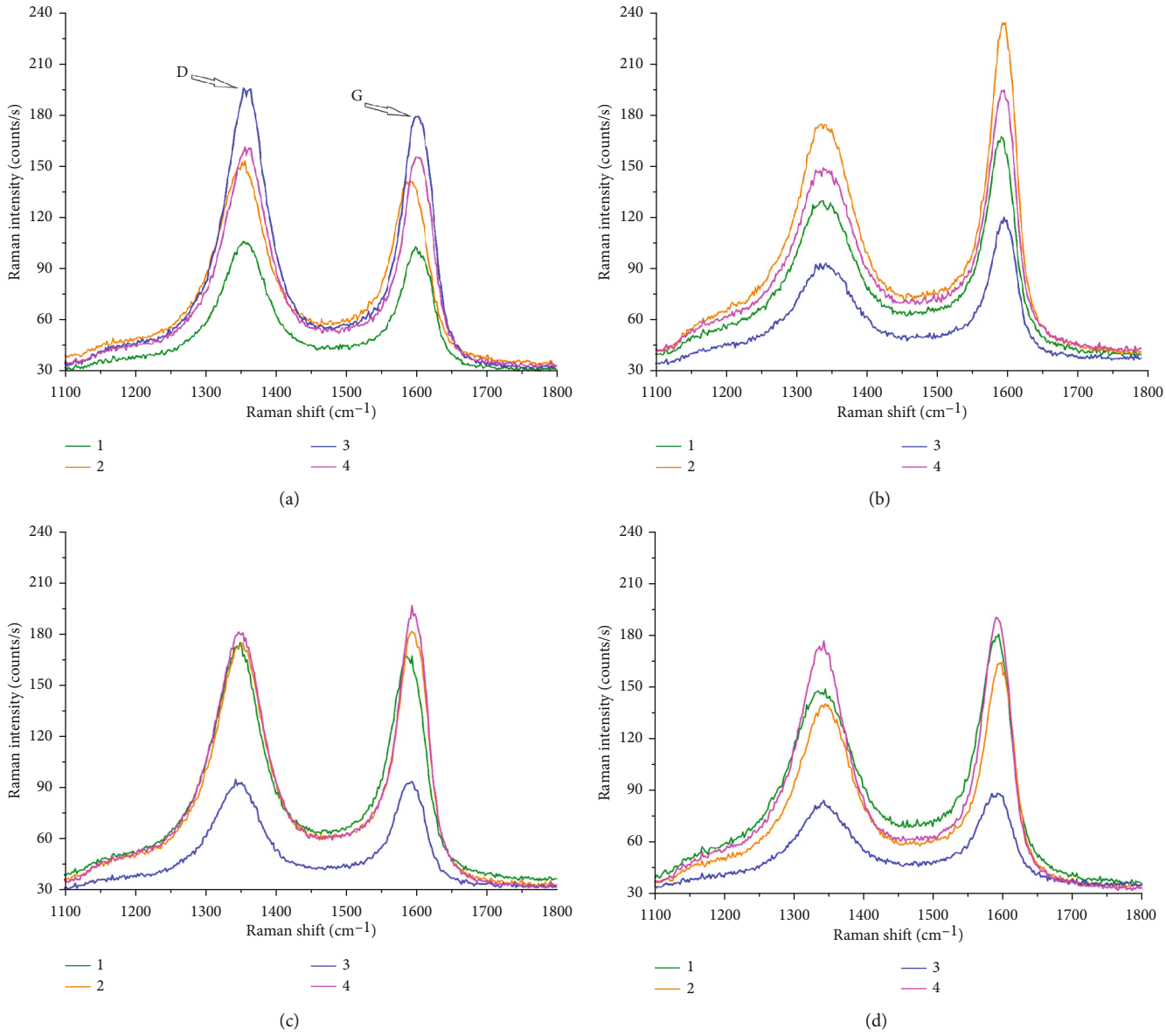

Figure 2: Raman spectra recorded for the samples of (a) EY1-50, (b) XD1-92, (c) BGP-12, and (d) JF-14."—1, 2, 3, 4" represents each test result of the samples. The Raman maturity of the sample can be calculated by reading peak G and peak D in each test and substituting them into Equation (1).

formed by solid bitumen thermal degradation is defined as compound pore herein. This solid bitumen fills the interlayer pores of clay minerals and dissolved pores of granular minerals (Figures 5(a)–5(d) and 5(f)).

Under the FE-SEM, various organic matter particles can be observed between mineral particles and clay minerals (Figures 4 and 5). The shale samples of CNF all have dense organic pores, but the pore sizes were various (Figure 4). The OM pores in the well EY1 sample are mainly circular pores of 5-10 nm in diameter, and some pores are about 50-100 nm in diameter. The size of OM pores in the XD1 well and JF profile increases. The pore sizes are typically 5-100 nm. The pore shapes are round and oval, and a small number of strips connected by two or three small pores. The main OM pore size of the BGP samples is slightly larger than that of the well EY1, but smaller than that of the JF samples. Simultaneously, when the contents of organic matter are high, the minerals are closely bound to organic matter (Figures 4–6). But some compound pores formed by solid asphalt and some minerals have larger apertures with 10-200 nm diameter, which are circular, oval, and irregular (Figure 5).

The main inorganic pores in CNF shale are dissolution pores and a few interP pores (Figure 5). The dissolution pores are of various shapes, including long strips parallel to each other (Figure 5(a)) and irregular distribution within the particles (Figures 5(a) and 5(c)–5(f)). In general, most of intraP and interP pores in the well EY1 samples are usually developed partially and poorly connected (Figures 5(a), 5(d), and 6(a)), while the intraP and interP pores in well XD1 are relatively well developed and have better connectivity (Figures 5(e), 5(f), and 6(b)). At the same time, in some samples, almost no pores can be seen in the view field (Figures 6(c) and 6(d)).

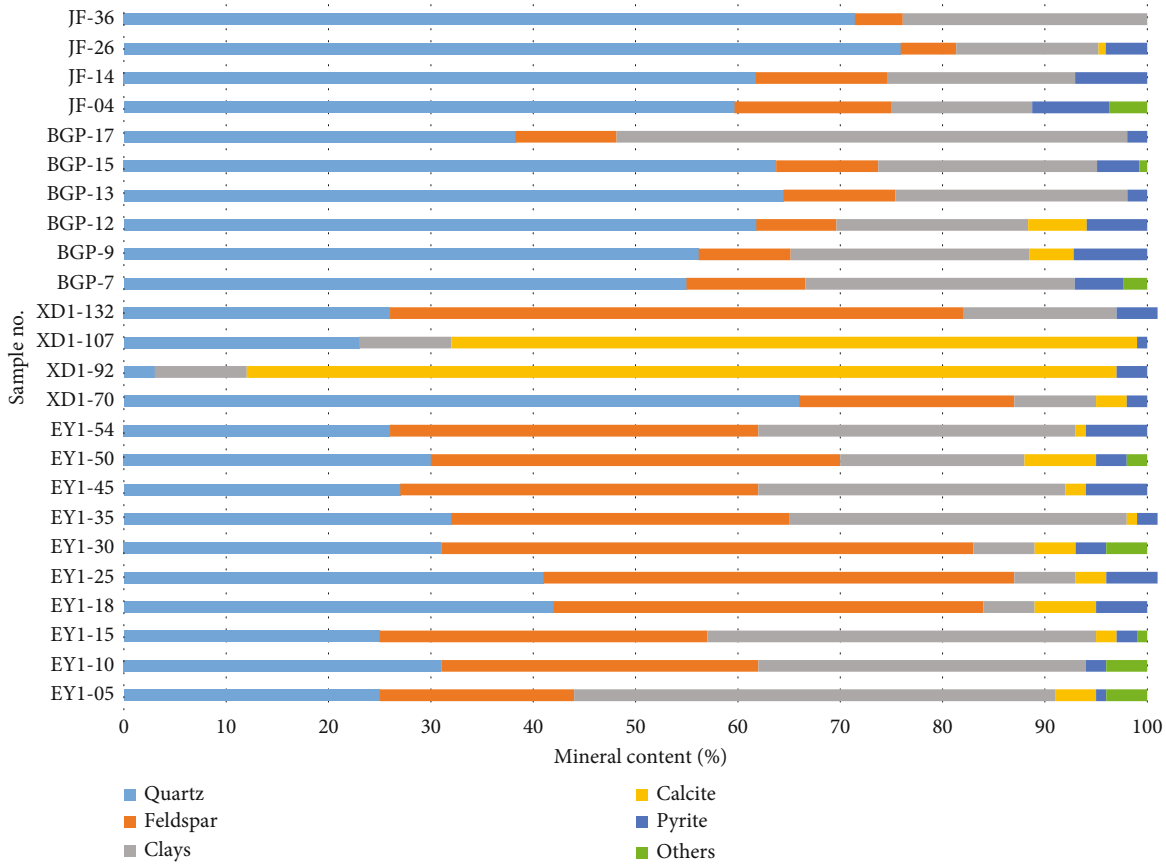

Figure 3: Distributions of the mineral compositions of the four groups of CNF shales.

There are some vertical fractures and high angle fractures in the core of well EY1, but no structural fractures are found under the FE-SEM. In general, the shale of the CNF mainly develops some diagenetic fractures at the contact between organic matter particles and large mineral particles and some dissolution fissures along the cleavage (Figures 5(a), 5(d), and 5(e)). These fractures are typically 1-5 μm long and 5-20 nm wide.

3.4. CO_2 and N_2 Adsorption Isotherms. Nanopores are generally classified as micropores (<2 nm), mesopores (2–50 nm), and macropores (>50 nm) according to the standard of the International Union of Pure and Applied Chemistry (IUPAC; [32]). Moreover, gas adsorption is an effective method to study nanopore types and structures in the shale [8, 9, 29, 33]. Sing et al. [32] had proposed that there were six types of isotherms and four types of hysteresis loops according to their shapes. According to the experimental results, the samples of the CNF exhibited the type IV isotherms and transitional hysteresis loops between H2 and H3, which illustrate there are many "ink bottle" pores (with narrow necks and wide bodies) and some slit-shaped pores [32] (Figure 7). Some samples like EY1-30 and JF-04, whose transitional hysteresis loops look more like H3, illustrate that there are more slit-shaped pores in the shales. Meanwhile, the samples like XD1-70 and BGP-13, whose transitional hysteresis loops look more like H2, illustrate that there are more "ink bottle" pores in the shale. Furthermore, almost all of the nitrogen adsorption curves of the CNF shale samples show that the adsorption and desorption curves do not coincide at lower pressures ($P/P_0 < 0.4$), Sing et al. [32] explained that this phenomenon was caused by the swelling of a nonrigid pore structure or with the irreversible uptake of molecules in pores (or through pore entrances). In other words, N_2 could not be desorbed properly after entering the micropores in this study.

The maximum N_2 adsorption capacity of shale samples is shown in Table 2. Test results show that (1) the samples from the JF profile have the highest maximum quantities adsorbed (MQAs) of N_2, ranging from 15.873 to 27.333 cm^3/g, with a mean of 22.560 cm^3/g. (2) The BGP samples have the second highest MQAs of N_2, which are in the range of 7.859-26.079 cm^3/g, with a mean of 17.649 cm^3/g. (3) The MQAs of XD1 well samples are in the range of 10.603-18.956 cm^3/g, with a mean of 15.632 cm^3/g. (4) The MQAs of EY1 well samples have the lowest MQAs of N_2, ranging from 5.090 to 16.809 cm^3/g with a mean of 11.505 cm^3/g.

The CO_2 adsorption curves of experimental samples are shown in Figure 8, which are consistent with the type I-microporous media adsorption curves in Sing et al. [32]. The samples from the JF profile have the highest MQAs of CO_2, varying from 3.985 to 4.772 $cm^{3/}g$, with a mean of 4.402 $cm^{3/}g$. The MQAs of BGP profile samples vary from

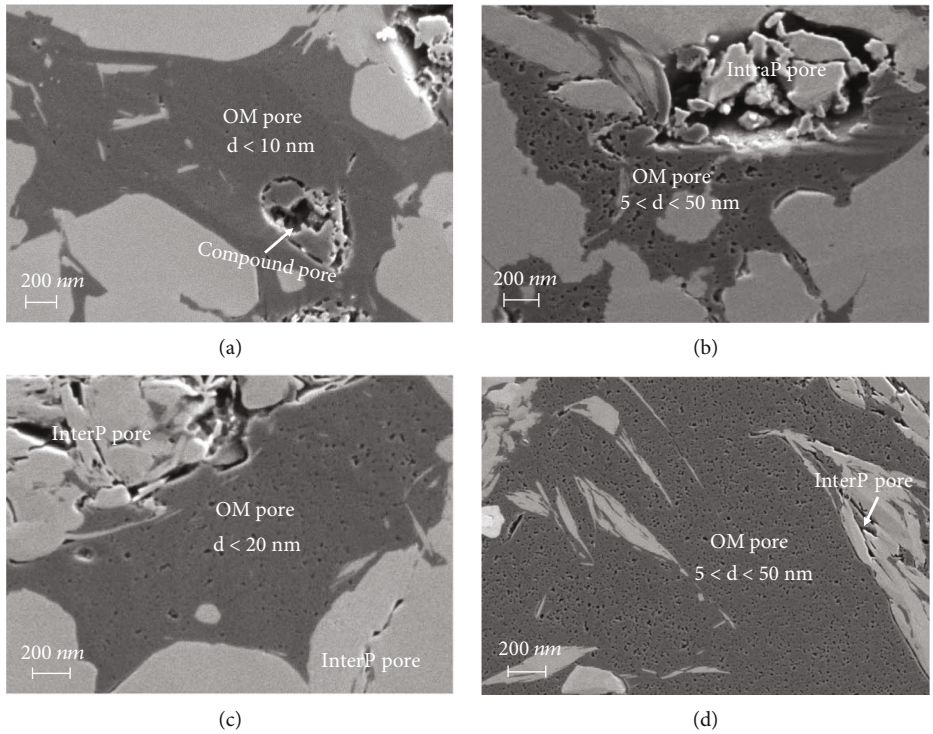

Figure 4: The FE-SEM images of organic pores in the CNF shale samples of the (a) EY1-18, (b) XD1-70, (c) BGP-12, and (d) JF-26 samples. The visible OM pores in the well EY1 profile sample are mainly circular pores of 5-10 nm in diameter. The visible OM pore size of BGP profile is slightly larger, but most of them do not exceed 20 nm. The OM pores in the well XD1 and JF profile sample are mainly circular pores of 5-100 nm in diameter.

2.816 to 5.567 $cm^{3/}g$, with a mean of 3.879 $cm^{3/}g$. The MQAs of XD1 well samples vary from 2.686 to 3.558 $cm^{3/}g$, with a mean of 3.124 $cm^{3/}g$. The MQAs of EY1 well samples vary from 3.148 to 4.713 cm^3/g, with a mean of 3.725 cm^3/g.

As mentioned above, CO_2 and N_2 adsorption measurements can provide pore structure parameters related to nanopores, such as pore volume, specific surface area, and pore size. Among them, the low-pressure N_2 adsorption method can effectively characterize the pores between 0.8 and 300 nm, which was the preferred method for studying the pore structure of organic-rich shale [8, 33, 34], while the low-pressure CO_2 adsorption was used to characterize the micropores that are smaller than 1.083 nm in this study.

The pore structure parameters are shown in Table 2. From the results of N_2 adsorption, the shales of EY1 well have the worst pore structure in the four groups of samples: (1) the minimum pore diameter of 6.660–15.342 nm, with an average of 10.877 nm; (2) the lowest surface area values, ranging from 2.292 to 14.174 m^2/g, with an average of 8.818 m^2/g; and (3) the minimum pore volume in the range of 0.685-2.508 $cm^3/100$ g, with an average of 1.694 $cm^3/100$ g. However, the results of CO_2 adsorption show that the well has a comparably higher micropore surface area and pore volume, with an average of 32.211 m^2/g and 0.287 $cm^3/100$ g, respectively.

In the N_2 adsorption measurement, the pore size of XD1 well exhibits a range of 10.345–16.038 nm, with an average of 13.777 nm. The surface area values range from 8.642 to 16.832 m^2/g, with an average of 11.648 m^2/g. The pore volume is in the range of 1.509-2.827 $cm^3/100$ g, with an average of 2.156 $cm^3/100$ g. In the CO_2 adsorption measurement, the XD1 well has the lowest micropore surface area and pore volume, with an average of 23.650 m^2/g and 0.250 $cm^3/100$ g, respectively.

Comparably, the BGP and JF profiles have better pore structure parameters in the N_2 adsorption measurement. The BGP profile have an average pore size of 18.074 nm, while the average pore size of the JF profile is 15.591 nm. The average surface area value of the BGP profile is 11.225 m^2/g, and that is 17.805 m^2/g for the JF profile. The average pore volume of the BGP profile is 2.446 $cm^3/100$ g. The JF profile is 3.174 $cm^3/100$ g. In the CO_2 adsorption measurement, the average surface area and pore volume of the BGP profile, respectively, are 30.766 m^2/g and 0.442 $cm^3/100$ g, which are 33.377 m^2/g and 0.505 $cm^3/100$ g for the JF profile samples.

Moreover, to better distinguish pore structure differences between the four groups of CNF samples, the CO_2 and N_2 adsorption amounts of different pore sizes of each sample were spliced together, and the proportion of adsorption amounts of different pores was calculated. The results are shown in Table 2 and Figure 9. The samples from the EY1 well have the highest micropore proportion with an average of 55.02%. The samples from the JF profile have a higher micropore proportion than the other two groups of shales, with an average of 46.28%. The samples from the XD1 well have the lowest micropore proportion, with an average of 33.44%. Overall, micropores smaller than 1 nm

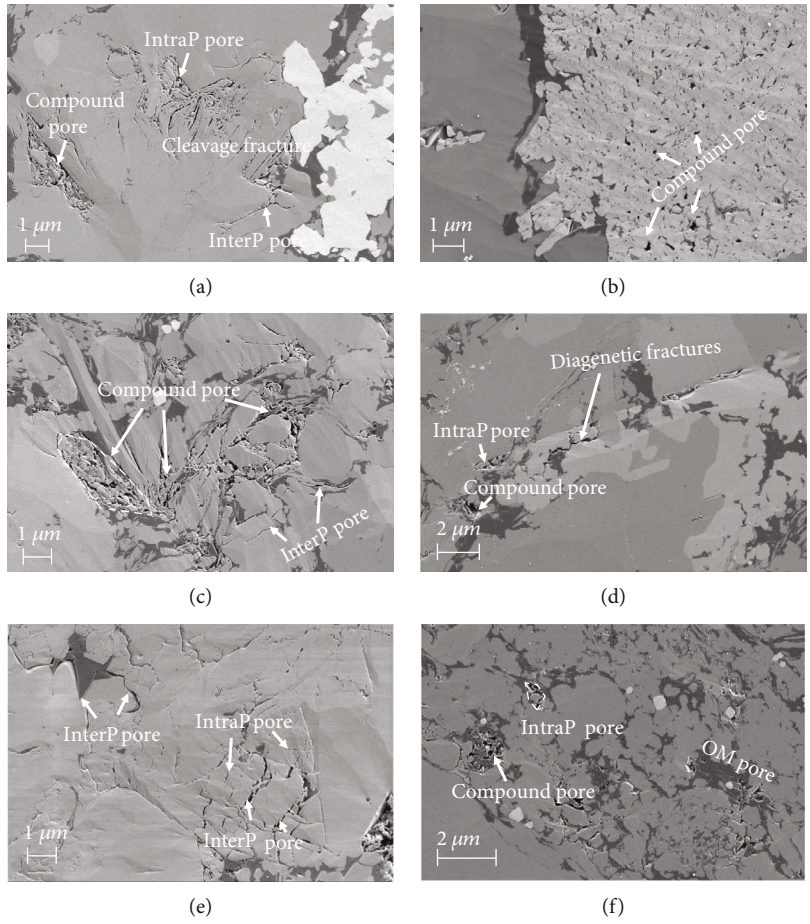

Figure 5: The FE-SEM images of organic and inorganic pores in the CNF shale samples of the (a) EY1-30, (b) EY1-45, (c) EY1-50, (d) EY1-35, (e) XD1-92, and (f) XD1-70. The main inorganic pores in the CNF shale are dissolution pores and a few interP pores.

are well developed in the CNF shale. Meanwhile, the mesopore and macropore development of JF and BGP profiles is better than that of EY1 and XD1 well (Figure 9).

4. Discussion

4.1. Pore Characteristics of Shales in the CNF. In this study, the nanopore signatures of the samples were studied by gas adsorption and FE-SEM observation. Under the FE-SEM, various organic matter particles distributed between mineral particles and clay minerals are observed. Organic pores from different wells or profiles are varied in size. The maximum pore size of almost OM pores is less than 100 nm. The inorganic pores of the four shale groups are mainly dissolution pores, some clay mineral interlayer pores, and composite pores. However, the overall development degree is worse than that of the Longmaxi shale in the Middle Yangtze region which was reported in Xu et al. [35]. At the same time, the connectivity of organic and inorganic pores in Niutitang shale is generally poor (Figures 5(d) and 5(f)).

According to the low-pressure gas adsorption measurement, four groups of CNF shale samples show their own pore structure characteristics. The N_2 adsorption mainly reflects the pore characteristics of meso-macropores in shale. The maximum N_2 adsorption capacities of the four groups of shale samples are different. The lowest mean value is 11.505 cm^3/g in the EY1 well while the highest is 22.56 cm^3/g in the JF profile (Table 2), indicating that the four groups of samples have developed different meso-macropores. CO_2 adsorption reflects the pore characteristics of micropores in shale. The average value of the CO_2 maximum adsorption capacity of the four groups of shale samples is greater than 3 cm^3/g. Comparatively, the CO_2 maximum adsorption capacity of the samples from lacustrine Yanchang Mudstone in Ordos Basin is no more than 2.0 cm^3/g [36], while it is mostly between 2.0 and 3.0 cm^3/g of the Longmaxi samples in the Middle Yangtze region [35]. The comparison results of CO_2 adsorption show that the micropores in CNF shales in this study area are well developed.

4.2. Main Formation Controlling Factors of Pore Structure. The pore structure of shales is affected by many factors. On the immature stage, it is mainly affected by early diagenesis. When the shale matures, the pore structure is more influenced by organic matter type, organic carbon content, mineral composition, the thermal evolution degree, and so on [3, 34, 37, 38]. In our study, the four groups of shale samples all are formed in the deep shelf environment (Figure 1(b)), which mainly contained the type I kerogen

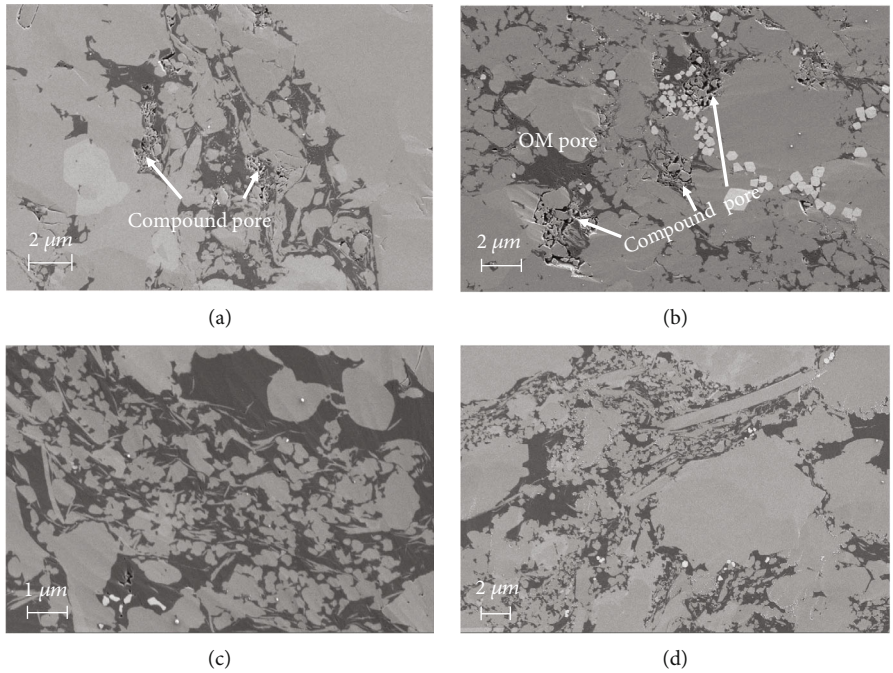

Figure 6: The FE-SEM images of organic and inorganic pores in the CNF shale samples of (a) EY1-18, (b) XD1-132, (c) EY1-05, and (d) EY1-15. The intraP and interP pores in well XD1 samples are relatively well developed and have better connectivity than them in well EY1. Meanwhile, in some samples, almost no pores can be seen in the view field.

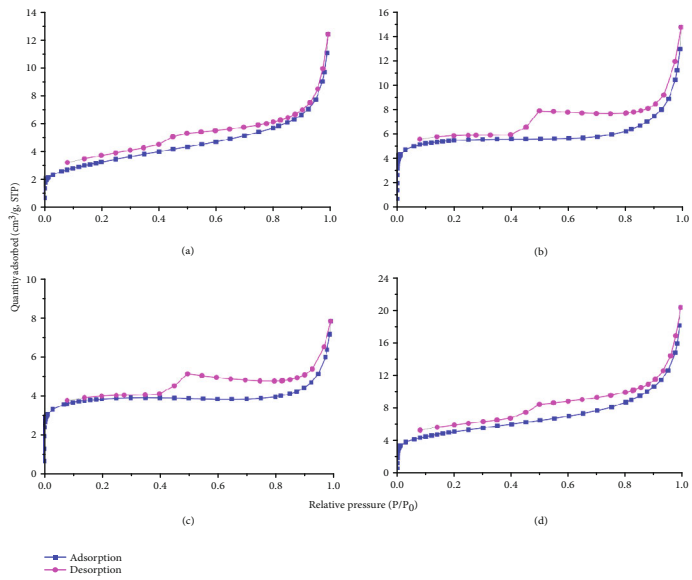

Figure 7: Low-pressure N_2 adsorption and desorption isotherms for the samples of (a) EY1-30, (b) XD1-70, (c) BGP-13, and (d) JF-04. These isotherms present all the tested CNF samples, illustrating that there are many "ink bottle" pores and slit-shaped pores in these samples.

[39]. Therefore, we will mainly discuss the influence of TOC content, thermal evolution degree, and mineral composition on the nanopores of the CNF shale.

4.2.1. Tectonic Uplift. Table 2 and Figure 9 exhibit difference in the nanopore characteristics of the four groups of the shales. The four groups of shales develop plentiful micropores; however, their mesopores and macropores develop quite differently. This is because the average MQAs of N_2 of the EY1 well is 11.505 cm^3/g and the average MQAs of N_2 of the BGP profile is 17.649 cm^3/g, while that of the XD1 well is 15.632 cm^3/g, and the JF profile is 22.560 cm^3/g.

As pointed out above, the EY1 well and BGP profile have approximately the same degree of evolution, with the $_{Rmc}R_0\%$ of 4.06% and 3.99%, respectively, while the $_{Rmc}R_0\%$ of the XD1 well and JF profile are 2.71% and 2.86%, respectively.

Table 2: The pore structure of shale samples measured by N_2 and CO_2 adsorption tests.

Sample no.	Average pore diameter (nm)	N_2 adsorption			CO_2 adsorption			N_2 & CO_2 adsorption			
		BET surface area (m^2/g)	BJH pore volume (cm^3/100 g)	Maximum adsorption capacity (cm^3/g)	DR surface area (m^2/g)	DFT pore volume (cm^3/100 g)	Maximum adsorption capacity (cm^3/g)	Total pore volume (cm^3/100 g)	Micropore proportion (%)	Mesopore proportion (%)	Macropore proportion (%)
EY1-05	14.792	2.292	0.685	5.142	38.273	0.121	3.148	0.639	44.22	24.78	31.00
EY1-10	9.970	11.503	2.292	15.451	30.878	0.318	3.790	1.144	50.77	20.53	28.70
EY1-15	15.342	3.694	0.696	5.090	40.352	0.410	4.713	1.065	63.28	17.70	19.02
EY1-18	12.588	8.230	1.933	13.094	27.608	0.279	3.229	1.289	47.28	24.40	28.33
EY1-25	11.125	8.585	1.661	11.524	35.084	0.399	4.265	1.176	60.97	15.79	23.25
EY1-30	6.660	11.279	2.029	12.426	31.583	0.236	3.671	0.752	62.44	24.09	13.47
EY1-35	10.303	8.695	1.519	10.665	27.099	0.251	3.249	0.900	52.73	19.95	27.33
EY1-45	9.236	8.260	1.391	9.650	29.750	0.272	3.653	0.756	62.52	15.01	22.48
EY1-50	7.925	14.174	2.222	15.194	33.549	0.348	4.169	1.129	63.81	21.19	15.00
EY1-54	10.832	11.464	2.508	16.809	27.931	0.240	3.363	1.232	42.21	24.84	32.95
XD1-70	16.038	16.832	1.634	14.775	27.595	0.274	3.470	2.373	37.29	29.95	32.76
XD1-92	15.414	9.719	2.827	18.956	19.196	0.168	2.686	1.867	17.66	39.70	42.64
XD1-107	13.310	11.400	2.656	18.195	25.419	0.370	3.558	1.920	36.67	31.23	32.10
XD1-132	10.345	8.642	1.509	10.603	22.391	0.186	2.782	0.977	42.15	28.49	29.36
BGP-7	26.450	11.861	3.067	22.187	44.553	0.697	5.567	3.944	36.67	30.04	33.29
BGP-9	17.926	14.109	2.988	21.715	32.580	0.471	4.239	3.024	35.44	30.00	34.56
BGP-12	14.185	19.612	3.560	26.079	30.698	0.426	4.042	3.068	34.68	31.02	34.30
BGP-13	11.163	11.858	0.743	7.859	23.947	0.330	3.172	1.382	59.24	20.20	20.56
BGP-15	19.733	7.045	2.964	19.405	28.375	0.343	3.436	2.571	27.45	32.58	39.97
BGP-17	18.989	2.862	1.355	8.652	24.445	0.265	2.816	1.233	35.27	28.15	36.58
JF-04	8.995	17.572	2.975	20.507	30.323	0.415	3.985	1.445	36.80	34.06	29.15
JF-14	7.984	27.151	3.692	26.528	36.448	0.574	4.772	1.996	34.69	34.16	31.15
JF-26	31.363	7.529	2.197	15.873	33.575	0.494	4.417	2.808	59.47	28.77	11.76
JF-36	14.024	18.970	3.832	27.333	33.162	0.538	4.435	3.223	54.14	29.02	16.84

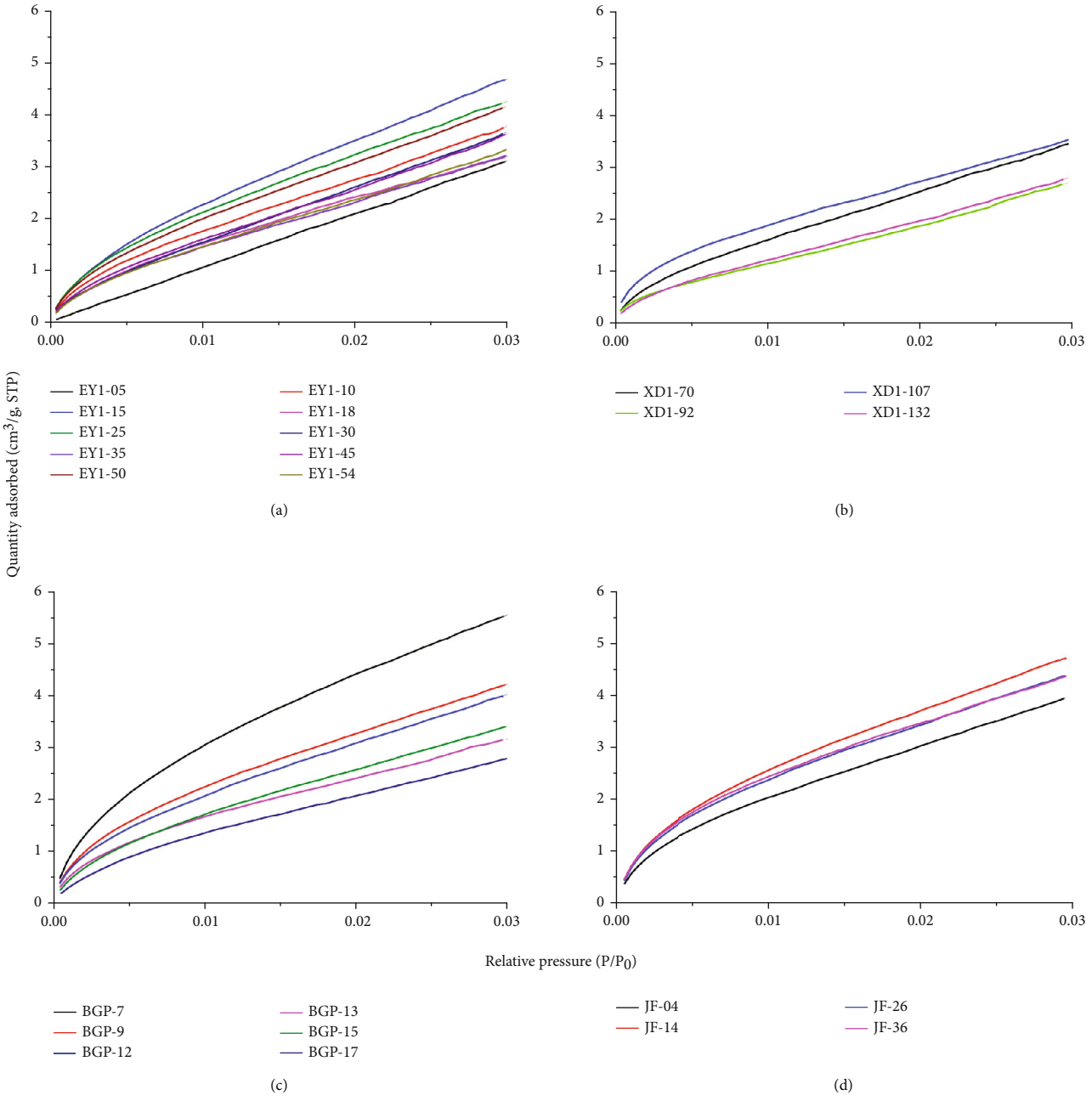

Figure 8: Low-pressure CO_2 adsorption isotherms of the four groups of the CNF shales: (a) is for the EY1 well tested samples, (b) is for the XD1 well tested samples, (c) is for the BGP profile tested samples, and (d) is for the JF profile tested samples.

Combined with the maturity and MQAs of N_2 of the four groups of samples, it can be seen that the MQAs of N_2 of the profile samples are significantly higher than those of the well samples with roughly the same maturity. Furthermore, based on the physical simulation experiment of diagenesis, Gao et al. [40] found that the "pore rebound" effect that occurred after tectonic uplift can increase the remaining primary pores of the reservoir by about 1%. This is because the formation cooling and pressure relief can lead to more diagenetic fracture in the reservoir which connect the remaining primary pores. Therefore, we inferred that tectonic uplift may be conducive to pressure release, making the holes that were once smaller due to burial compaction become larger.

4.2.2. Maturity of Organic Matter. With the increase of burial depth, inorganic pores generally decrease constantly because of compaction. At the same time, the organic matter stored in shales goes through the evolution stages from immature to mature, then to high mature, and finally to overmature, which are corresponding to formation of kerogen, kerogen cracking during oil and gas generation and expulsion, condensation of residual liquid hydrocarbon into solid asphalt, and finally secondary cracking of kerogen and solid asphalt to form methane [41, 42]. In this process, the OM pores in the shales are not developed firstly. Subsequently, the OM pores are occupied by liquid hydrocarbon. Finally, a large number of OM pores are formed by pyrolysis

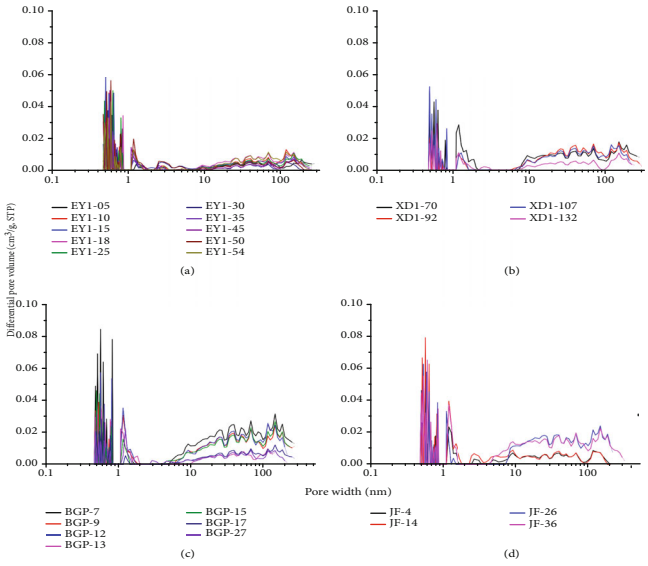

FIGURE 9: The pore volume distribution of the four groups of CNF shales: (a) is for the EY1 well tested samples, (b) is for the XD1well tested samples, (c) is for the BGP profile tested samples, and (d) is for the JF profile tested samples. The results show that profile samples have more micro-, meso-, and macropores than core samples.

gas [3, 43–45]. However, some exploration practices found that the organic-rich shale with $R_o > 3.5\%$ generally has no pores [44, 46]. This is because when the shale is overmatured, the organic matter is densified by a condensation reaction [43]. Therefore, the development of organic pores in shale is closely related to its maturity.

In this study, one or two samples from each well or section are selected for Raman spectroscopy. The results are exhibited in Table 2. The ${}_{\text{Rmc}}R_0\%$ are ca. 4% for the EY1 well and BGP profile samples and ca. 2.8% and 2.7% for the JF profile and XD1 well samples, respectively. To exclude the influence of structural uplift on pore structure, the samples of the same type were compared. Through comparative study, it is found that the XD1 well and JF profile samples with lower maturity had larger OM pores while the BGP profile and EY1 well samples with higher evolution have significantly smaller organic pores (Figure 4). In addition, we also find that the maximum adsorption of N_2 of samples is overall negatively correlated with its maturity. In other words, the maturity of the JF profile is lower and its N_2 adsorption capacity is larger while the maturity of the BGP profile is higher and its N_2 adsorption capacity is lower. Meanwhile, the N_2 adsorption capacity of the XD1 well is larger when the maturity is lower, and the N_2 adsorption capacity of the well EY1 is smaller when the maturity is higher.

However, the EY1 well which has the highest maturity also has some samples with large N_2 adsorption capacity, e.g., EY1-10, EY-50, and EY1-54, while the XD1 well also has a sample with low N_2 adsorption capacity, e.g., XD1-132, indicating that the maturity is not the only influence factor on porosity. Therefore, other influencing factors will be discussed next.

4.2.3. TOC Content. OM pores play an important part in the reservoir space of mature shale [18, 44, 47]. After shale enters the mature stage ($R_o > 0.6$), OM is consumed and transformed into hydrocarbons with the increase of maturity. Meanwhile, the OM pores increase accordingly which offer surface area and pore volume [33, 44, 45]. Previous studies have shown that when the same type of organic matter has the same maturity, porosity and TOC had a piecewise relationship; i.e., when the TOC is below a certain value, porosity and TOC have a positive correlation. When the TOC is above a certain value, the correlation would become negative for its plasticity [43, 48–50]. In general, the TOC content controls the development of organic pores and affects the pore size in different ranges.

To study the influence of the organic contents on shale pores in this group, the gas adsorption data of the samples in this study were fitted to their TOC content, as shown in Figure 10. The results show that TOC contents have no relationship with the total pore volume or the N_2 maximum adsorption capacity of all the samples, but a positive correlation exists between the total pore volume and the N_2 maximum adsorption capacity of the JF profile and XD1 well. Meanwhile, the TOC contents have a strong positive correlation with the CO_2 maximum adsorption capacity, a weak positive correlation with the proportion of micropores, and some negative correlation with the proportion of mesopores and macropores. In this study, N_2 adsorption characterized the pores between 1.083 and 300 nm, and CO_2 adsorption characterized micropores smaller than 1.083 nm. Therefore, according to the relational graph, the SEM photograph, and some previous research results, we can infer that (1) there is no piecewise relationship between TOC contents and pore volume in the study area probably because almost all of their TOC contents are high, and the maturity of the four groups of samples is different (Figure 10(a)). (2) Though there is no relationship between TOC contents and pore volume of all the samples (Figure 10(b)), there is a positive correlation between the total pore volume and the N_2 maximum adsorption capacity of the JF profile and XD1 well (Figures 10(c) and 10(d)), which is consistent with the FE-SEM photograph, that most of OM pore sizes of the experimental samples in the study area are small (mainly less than 5 nm). Nevertheless, there are large OM pores developed in the XD1 well and JF profile ranging from 5 to 100 nm that partly contribute to the pore volume (Figure 4). However, the correlation coefficient is not high, indicating that the other factors have more influence on the development of mesopores and macropores. (3) The OM of shale samples in the study area provides many micropores smaller than 1.083 nm inferred form the strong positive correlation between TOC contents and CO_2 maximum adsorption capacity (Figure 10(e)). However, the correlation coefficient between TOC contents and micropore proportion which contains all micropores is decreased (Figure 10(f)). Consequently, we deem that some micropores between 1.083 and 2 nm are inorganic pores from these two groups of relationships (Figures 10(e) and 10(f)). (4) The increase of OM would reduce the corresponding mineral particles; moreover, the OM is a soft and plastic

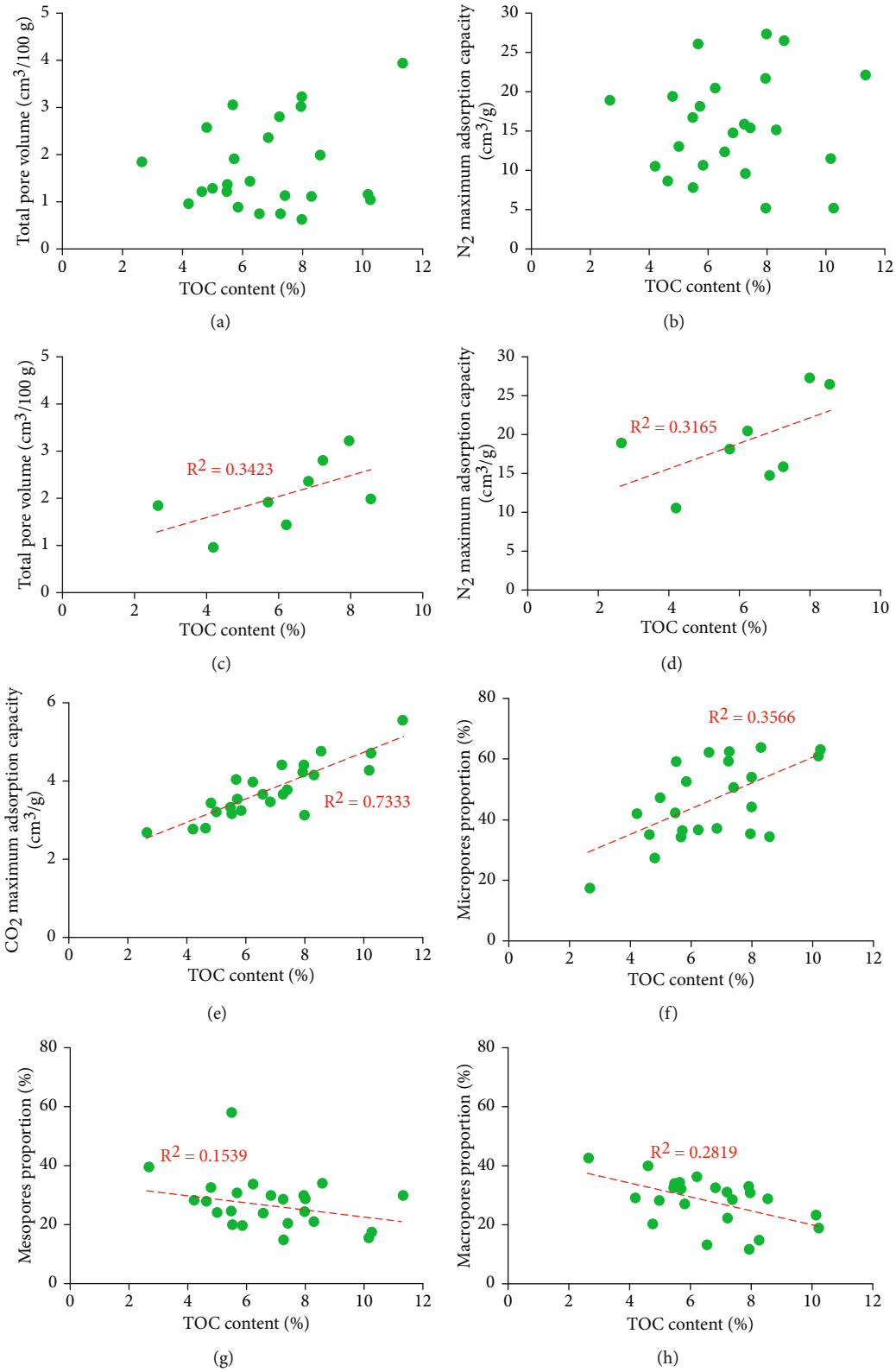

Figure 10: The correlation between TOC and pore structure: (a) is for the total pore volume and TOC contents of the all tested samples, (b) is for the N_2 maximum adsorption capacity and TOC contents of the all tested samples, (c) is for the total pore volume and TOC contents of the JF profile and XD1 well tested samples, (d) is for the N_2 maximum adsorption capacity and TOC contents of the JF profile and XD1 well tested samples, (e) is for the CO_2 maximum adsorption capacity and TOC contents of the all tested samples, (f) is for the micropore proportion and TOC contents of the all tested samples, (g) is for the mesopore proportion and TOC contents of the all tested samples, and (h) is for the macropore proportion and TOC contents of the all tested samples.

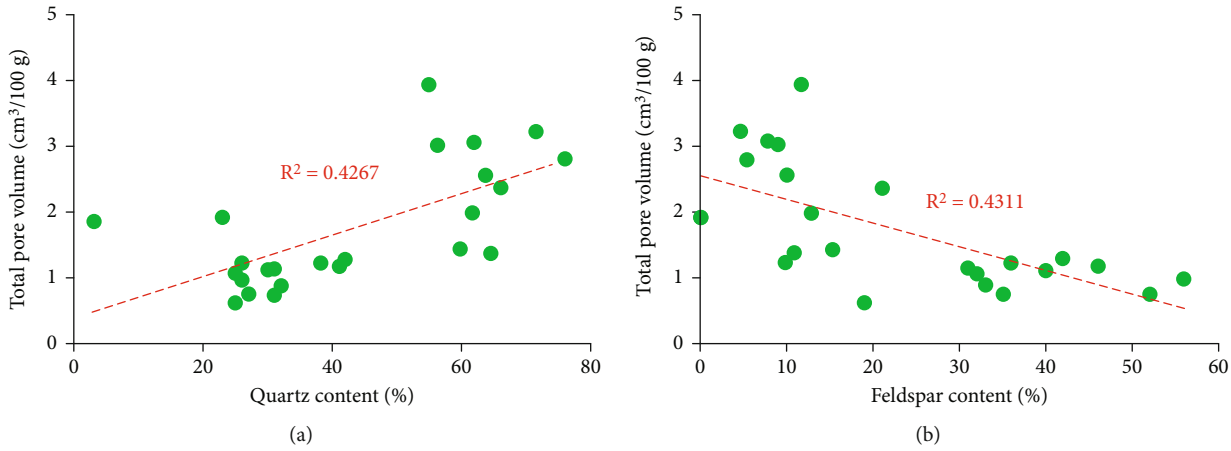

Figure 11: The correlation between minerals and adsorption data: (a) is for the total pore volume and quartz content, and (b) is for the total pore volume and feldspar content.

particle with poor compressive ability. When the OM is overmature and lost its hydrocarbon generation capacity and has been under the burial pressure of shale in a long geological history, the volume of meso-macropores in shale would gradually decrease due to the weak compressive ability of rock page. Thus, there is a weak negative correlation between TOC contents and the proportion of mesopores and macropores (Figures 10(f) and 10(h)).

4.2.4. Mineral Compositions. The main mineral components of the CNF shale in the study area are quartz, feldspar, clay minerals, calcite, and a small amount of pyrite. According to previous research results, all of these minerals have different effects on shale pores [6, 34, 44, 51]. The inorganic pores of the four shale groups in this study are mainly dissolution pores, some clay mineral interlayer pores, and clay mineral composite pores (Figure 5). Due to the high TOC contents of the samples, the practice of energy spectrum analysis by the FE-SEM was not good. Thus, the mineral identification was mainly analyzed by combining XRD diffraction results and mineral color morphology. To discuss the influence of mineral composition on the pore structure of shale, the adsorption data in Table 2 were fitted to the mineral composition data in Table 1. However, the results show that only quartz and feldspar contents were positively and negatively correlated with the total pore volume, respectively (Figure 11), while the other minerals had no relationship with the adsorption data.

Figure 11(a) exhibits the effect of quartz on pore construction; i.e., high quartz content is conducive to the development of shale pores. This is because quartz is the mineral with the strongest weathering resistance and highest hardness among detrital minerals. The increase of its contents leads to the stronger compressive resistance of shale in diagenesis and the preservation of shale pores. But Figure 11(b) shows the destructive effect of feldspar on pores. The higher their contents, the lower the pore volume. Under acidic conditions, feldspar and water will heterogeneously dissolve. However, when the dissolution reaction occurs, in addition to the formation of dissolution pores, the reaction will also form one or more new mineral or amorphous solid materials. Due to the different physical and chemical properties, such as molecular weight and density, the newly generated minerals or solids occupy different volume spaces [52]. Although feldspar can be dissolved, no new dissolution pore would be formed again because of the limit of organic acid generated in the process of hydrocarbon generation and the densification of shale reservoir, when the acidic fluid is saturated. Therefore, the more the feldspar, the lower the pore volume. Furthermore, we obtain the speculation of the effect of other minerals on the pores of the CNF shale through Tables 1 and 2 and FE-SEM observation although we did not obtain the effect of other minerals on the pores in the adsorption data and mineral fitting. Firstly, there are two samples with the smallest N_2 adsorption in well EY1 (EY1-05 and EY1-15). Through the study of their mineral composition, it was found that the contents of clay minerals and the TOC in the two samples are high. Both these two components are characterized by softness and plastic. Of course, under the FE-SEM, there is scarcely pore development in some of the field of view (Figures 6(c) and 6(d)). Therefore, it can be concluded that the higher the content of soft components, the worse the pore structure is in shale samples of the CNF with high maturity. Secondly, the three samples with the highest nitrogen adsorption capacity in the EY1 well are observed and studied. It is found that even though the content of organic carbon is high in the highly evolved samples, the dissolution pores are relatively developed and the content of granular minerals is high (the contents of samples are higher than 60%). The meso-macropores of these samples are still relatively developed, so the maximum nitrogen adsorption capacity is high.

5. Conclusions

In this study, the laser Raman, X-ray diffraction analysis, FE-SEM, and low-pressure N_2 and CO_2 adsorption were used to study the geochemical characteristics, mineral composition characteristics, and pore characteristics of the CNF shale in the Middle Yangtze region and to analyze the controlling

factors of pore formation. The following conclusions are drawn:

(1) The TOC contents of organic-rich shale selected in this study ranged from 2.65 to 11.33%, with an average of 6.81%. The main mineral components of these samples in the study area are quartz, feldspar, clay minerals, calcite, and a small amount of pyrite. Two of the samples are argillaceous limestone. The $_{\mathrm{Rmc}}R_0$% of the JF profile and XD1 well samples are about 2.8% and 2.7%, while the $_{\mathrm{Rmc}}R_0$% of the BGP profile and EY1 well samples are about 3.99% and 4.06%

(2) The N_2 adsorption of field profile samples is higher than that of well samples, which demonstrate that the tectonic uplift releases the pressure and improves the pore structure. Meanwhile, the comparison of the maximum N_2 adsorption capacity of similar samples shows that the samples with lower evolution degrees have higher nitrogen adsorption capacity while the samples with higher evolution degrees have lower maximum N_2 adsorption capacity

(3) OM pores from different wells or field profiles varied in size. The maximum pore size of almost OM pores is not more than 100 nm. The XD1 well and JF profile samples have larger OM pore sizes (10 to 100 nm) than those of the EY1 well and BGP profile samples (barely exceeding 10 nm). The maturity is the key factor leading to the difference in OM pores among four groups of shales. Furthermore, in the CNF shales with the same maturity, the higher the TOC content, the more the micropores developed, and the less the meso-macropores developed

(4) The EY1 well with the highest maturity also has some samples with large N_2 adsorption capacity, while the XD1 well with the relatively lower maturity also has a sample with low N_2 adsorption capacity, indicating that the maturity is not the only influence factor on porosity. The FE-SEM observation and mineral composition analysis show that the dissolution pores and granular mineral support are also the key factors for the better pore structure of the high-evolution CNF shale while the high contents of TOC and clay minerals lead to poor pore structure of the relatively lower evolution shales

Data Availability

The majority of the data used to support the findings of this study are included within the article.

Conflicts of Interest

The authors declare that they have no conflicts of interest.

Acknowledgments

This research is supported by the Doctoral Research Fund of Lanzhou University (No. LZCU-BS2022-06) and Natural Science Foundation of Jiangxi Province (20192BAB213025).

References

[1] J. B. Curtis, "Fractured shale-gas systems," *AAPG Bulletin*, vol. 86, no. 11, pp. 1921–1938, 2002.

[2] C. Zou, D. Dong, S. Wang et al., "Geological characteristics and resource potential of shale gas in China," *Petroleum Exploration and Development*, vol. 37, no. 6, pp. 641–653, 2010.

[3] J. Chen and X. Xiao, "Evolution of nanoporosity in organic-rich shales during thermal maturation," *Fuel*, vol. 129, pp. 173–181, 2014.

[4] L. T. Ko, R. G. Loucks, T. Zhang, S. C. Ruppel, and D. Shao, "Pore and pore network evolution of Upper Cretaceous Boquillas (Eagle Ford–equivalent) mudrocks: results from gold tube pyrolysis experiments," *AAPG Bulletin*, vol. 100, no. 11, pp. 1693–1722, 2016.

[5] L. T. Ko, S. C. Ruppel, R. G. Loucks, P. C. Hackley, T. Zhang, and D. Shao, "Pore-types and pore-network evolution in Upper Devonian-Lower Mississippian Woodford and Mississippian Barnett mudstones: insights from laboratory thermal maturation and organic petrology," *International Journal of Coal Geology*, vol. 190, pp. 3–28, 2018.

[6] U. Kuila, D. K. McCarty, A. Derkowski, T. B. Fischer, T. Topór, and M. Prasad, "Nano-scale texture and porosity of organic matter and clay minerals in organic-rich mudrocks," *Fuel*, vol. 135, pp. 359–373, 2014.

[7] A. Ghanizadeh, M. Gasparik, A. Amann-Hildenbrand, Y. Gensterblum, and B. M. Krooss, "Lithological controls on matrix permeability of organic-rich shales: an experimental study," *Energy Procedia*, vol. 40, pp. 127–136, 2013.

[8] C. R. Clarkson, N. Solano, R. M. Bustin et al., "Pore structure characterization of North American shale gas reservoirs using USANS/SANS, gas adsorption, and mercury intrusion," *Fuel*, vol. 103, pp. 606–616, 2013.

[9] T. Cao, Z. Song, S. Wang, X. Cao, Y. Li, and J. Xia, "Characterizing the pore structure in the Silurian and Permian shales of the Sichuan Basin, China," *Marine and Petroleum Geology*, vol. 61, pp. 140–150, 2015.

[10] X. Zhang, W. Shi, G. Zhai et al., "Characteristics and controlling factors of shale gas reservoir in the Fuling area, Sichuan Basin," *Petroleum Research*, vol. 2, no. 1, pp. 25–40, 2017.

[11] D. Dong, Y. Wang, X. Huang et al., "Discussion about geological characteristics, resource evaluation methods and its key parameters of shale gas in China," *Natural Gas Geoscience*, vol. 27, no. 9, pp. 1583–1601, 2016.

[12] M. Zheng, J. Li, W. Xiaozhi et al., "China's conventional and unconventional natural gas resource potential, key exploration fields and direction," *Natural Gas Geoscience*, vol. 29, no. 10, pp. 1383–1397, 2018.

[13] P. Wang, Z. Jiang, L. Chen et al., "Pore structure characterization for the Longmaxi and Niutitang shales in the Upper Yangtze Platform, South China: evidence from focused ion beam-He ion microscopy, nano-computerized tomography and gas adsorption analysis," *Marine and Petroleum Geology*, vol. 77, pp. 1323–1337, 2016.

[14] P. Wang, S. Yao, C. Jin et al., "Key reservoir parameter for effective exploration and development of high-over matured marine shales: a case study from the Cambrian Niutitang formation and the Silurian Longmaxi Formation, south China," *Marine and Petroleum Geology*, vol. 121, article 104619, 2020.

[15] Z. Xi, S. Tang, J. Li, Z. Zhang, and H. Xiao, "Pore characterization and the controls of organic matter and quartz on pore structure: case study of the Niutitang Formation of northern Guizhou Province, South China," *Journal of Natural Gas Science and Engineering*, vol. 61, pp. 18–31, 2019.

[16] D. Liu, X. Xiao, H. Tian et al., "Sample maturation calculated using Raman spectroscopic parameters for solid organics: methodology and geological applications," *Chinese Science Bulletin*, vol. 58, no. 11, pp. 1285–1298, 2013.

[17] R. G. Loucks, R. M. Reed, S. C. Ruppel, and D. M. Jarvie, "Morphology, genesis, and distribution of nanometer-scale pores in siliceous mudstones of the Mississippian Barnett shale," *Journal of Sedimentary Research*, vol. 79, no. 12, pp. 848–861, 2009.

[18] R. G. Loucks, R. M. Reed, S. C. Ruppel, and U. Hammes, "Spectrum of pore types and networks in mudrocks and a descriptive classification for matrix-related mudrock pores," *AAPG Bulletin*, vol. 96, no. 6, pp. 1071–1098, 2012.

[19] D. M. Jarvie, R. J. Hill, T. E. Ruble, and R. M. Pollastro, "Unconventional shale-gas systems: the Mississippian Barnett Shale of north-central Texas as one model for thermogenic shale-gas assessment," *AAPG Bulletin*, vol. 91, no. 4, pp. 475–499, 2007.

[20] J. Tuo, W. Chenjun, and M. Zhang, "Organic matter properties and shale gas potential of Paleozoic shales in Sichuan Basin, China," *Journal of Natural Gas Science and Engineering*, vol. 28, pp. 434–446, 2016.

[21] Q. Luo, G. Fariborz, N. Zhong et al., "Graptolites as fossil geothermometers and source material of hydrocarbons: an overview of four decades of progress," *Earth-Science Reviews*, vol. 200, article 103000, 2020.

[22] C. Caricchi, S. Corrado, L. Di Paolo, L. Aldega, and D. Grigo, "Thermal maturity of Silurian deposits in the Baltic Syneclise (on-shore Polish Baltic Basin): contribution to unconventional resources assessment," *Società Geologica Italiana*, vol. 135, no. 3, pp. 383–393, 2016.

[23] Q. Zhou, X. Xiao, L. Pan, and H. Tian, "The relationship between micro-Raman spectral parameters and reflectance of solid bitumen," *International Journal of Coal Geology*, vol. 121, pp. 19–25, 2014.

[24] B. Sauerer, P. R. Craddock, M. D. AlJohani, K. L. Alsamadony, and W. Abdallah, "Fast and accurate shale maturity determination by Raman spectroscopy measurement with minimal sample preparation," *International Journal of Coal Geology*, vol. 173, pp. 150–157, 2017.

[25] B. Sauerer, A. Furmann, A. Fernandes et al., "Assessing extreme maturities - challenging examples from immature Jordanian to overmature Far Eastern unconventional formations," *Marine and Petroleum Geology*, vol. 129, article 105103, 2021.

[26] D. G. Henrya, I. Jarvis, G. Gillmore, and M. Stephenson, "Raman spectroscopy as a tool to determine the thermal maturity of organic matter: application to sedimentary, metamorphic and structural geology," *Earth-Science Reviews*, vol. 198, article 102936, 2019.

[27] J. S. Lupoi, P. C. Hackley, E. Birsic et al., "Quantitative evaluation of vitrinite reflectance in shale using Raman spectroscopy and multivariate analysis," *Fuel*, vol. 254, article 115573, 2019.

[28] A. Schito, C. Romano, S. Corrado, D. Grigo, and B. Poe, "Diagenetic thermal evolution of organic matter by Raman spectroscopy," *Organic Geochemistry*, vol. 106, pp. 57–67, 2017.

[29] L. Chen, Z. Jiang, K. Liu, J. Tan, F. Gao, and P. Wang, "Pore structure characterization for organic-rich Lower Silurian shale in the Upper Yangtze Platform, South China: a possible mechanism for pore development," *Journal of Natural Gas Science and Engineering*, vol. 46, pp. 1–15, 2017.

[30] S. Bernard, B. Horsfield, H.-M. Schulz et al., "Multi-scale detection of organic and inorganic signatures provides insights into gas shale properties and evolution," *Chemie der Erde-Geochemistry*, vol. 70, pp. 119–133, 2010.

[31] T. Dong, N. B. Harris, K. Ayranci, C. E. Twemlow, and B. R. Nassichuk, "Porosity characteristics of the Devonian Horn River shale, Canada: insights from lithofacies classification and shale composition," *International Journal of Coal Geology*, vol. 141-142, pp. 74–90, 2015.

[32] K. S. W. Sing, D. H. Everett, R. A. W. Haul et al., "Reporting physisorption data for gas/solid systems with special reference to the determination of surface area and porosity (recommendations 1984)," *Pure and Applied Chemistry*, vol. 57, no. 4, pp. 603–619, 1985.

[33] M. Mastalerz, A. Schimmelmann, A. Drobniak, and Y. Chen, "Porosity of Devonian and Mississippian New Albany Shale across a maturation gradient: insights from organic petrology, gas adsorption, and mercury intrusion," *AAPG Bulletin*, vol. 97, no. 10, pp. 1621–1643, 2013.

[34] D. J. K. Ross and R. Marc Bustin, "The importance of shale composition and pore structure upon gas storage potential of shale gas reservoirs," *Marine and Petroleum Geology*, vol. 26, no. 6, pp. 916–927, 2009.

[35] J. Xu, W. Guo, H. Liu, Z. Qin, Q. Meng, and H. Tao, "Micropore structure characteristics and quantitative characterization of Silurian Longmaxi shale in western Hubei and Hunan areas," *Natural Gas Geoscience*, vol. 32, no. 4, pp. 611–622, 2021.

[36] S. Li, Y. Wang, X. Wang, and R. Guo, "Pore system and gas adsorption potential of lacustrine Yanchang Mudstone, Ordos Basin, China," *Energy Reports*, vol. 8, pp. 571–581, 2022.

[37] G. R. Chalmers, R. Marc Bustin, and I. M. Power, "Characterization of gas shale pore systems by porosimetry, pycnometry, surface area, and field emission scanning electron microscopy/transmission electron microscopy image analyses: examples from the Barnett, Woodford, Haynesville, Marcellus, and Doig units," *AAPG Bulletin*, vol. 96, no. 6, pp. 1099–1119, 2012.

[38] Y. Wang, Y. Zhu, S. Chen, and W. Li, "Characteristics of the nanoscale pore structure in northwestern Hunan shale gas reservoirs using field emission scanning electron microscopy, high-pressure mercury intrusion, and gas adsorption," *Energy & Fuels*, vol. 28, no. 2, pp. 945–955, 2014.

[39] D. Liang, T. Guo, J. Chen, L. Bian, and Z. Zhao, "Some progresses on studies of hydrocarbon generation and accumulation in marine sedimentary regions, southern China (part 2): geochemical characteristics of four suits of regional marine source rocks, South China," *Marine Origin Petroleum Geology*, vol. 14, no. 1, pp. 1–15, 2009.

[40] Z. Gao, J. Cui, J. Feng, C. Zhou, and Y. Shi, "Sandstone pore rebounding evolution model of a geological process from burial compaction to tectonic uplift," *Chinese Journal of Geology*, vol. 53, no. 2, pp. 531–546, 2018.

[41] C. C. Walters, H. Freund, S. R. Kelemen, P. Peczak, and D. J. Curry, "Predicting oil and gas compositional yields via

chemical structure-chemical yield modeling (CS-CYM): part 2 - application under laboratory and geologic conditions," *Organic Geochemistry*, vol. 38, no. 2, pp. 306–322, 2007.

[42] M. Erdmann and B. Horsfield, "Enhanced late gas generation potential of petroleum source rocks via recombination reactions: evidence from the Norwegian North Sea," *Geochimica et Cosmochimica Acta*, vol. 70, no. 15, pp. 3943–3956, 2006.

[43] T. Borjigin, L. Lu, L. Yu et al., "Formation, preservation and connectivity control of organic pores in shale," *Petroleum Exploration and Development*, vol. 48, no. 4, pp. 798–812, 2021.

[44] M. E. Curtis, B. J. Cardott, C. H. Sondergeld, and C. S. Rai, "Development of organic porosity in the Woodford Shale with increasing thermal maturity," *International Journal of Coal Geology*, vol. 103, pp. 26–31, 2012.

[45] S. Bernard, R. Wirth, A. Schreiber, H.-M. Schulz, and B. Horsfield, "Formation of nanoporous pyrobitumen residues during maturation of the Barnett Shale (Fort Worth Basin)," *International Journal of Coal Geology*, vol. 103, pp. 3–11, 2012.

[46] X. Xiao, M. Wang, Q. Wei, H. Tian, L. Pan, and T. Li, "Evaluation of Lower Paleozoic Shale with shale gas prospect in South China," *Natural Gas Geoscience*, vol. 26, no. 8, pp. 1433–1445, 2015.

[47] H. Tian, L. Pan, X. Xiao, R. W. T. Wilkins, Z. Meng, and B. Huang, "A preliminary study on the pore characterization of Lower Silurian black shales in the Chuandong Thrust Fold Belt, southwestern China using low pressure N_2 adsorption and FE-SEM methods," *Marine and Petroleum Geology*, vol. 48, pp. 8–19, 2013.

[48] K. L. Milliken, M. Rudnicki, D. N. Awwiller, and T. Zhang, "Organic matter-hosted pore system, Marcellus Formation (Devonian), Pennsylvania," *AAPG Bulletin*, vol. 97, no. 2, pp. 177–200, 2013.

[49] L. Pan, X. Xiao, H. Tian et al., "A preliminary study on the characterization and controlling factors of porosity and pore structure of the Permian shales in Lower Yangtze region, Eastern China," *International Journal of Coal Geology*, vol. 146, pp. 68–78, 2015.

[50] R. Wang, D. Gong, J. Leng et al., "Developmental characteristics of the Lower Cambrian Niutitang shale reservoir in Northern Guizhou area: a case study in the Cengong block," *Earth Science Frontiers*, vol. 24, no. 6, pp. 286–299, 2017.

[51] Z. Wei, Y. Wang, G. Wang, Z. Suna, and X. Liang, "Pore characterization of organic-rich late Permian Da-long Formation shale in the Sichuan Basin, southwestern China," *Fuel*, vol. 211, pp. 507–516, 2018.

[52] W. Li, X. Zhang, and Y. Zhong, "Formation mechanism of secondary dissolved pores in arcose," *Oil &Gas Geology*, vol. 26, no. 2, pp. 220–223, 2005.